https://doi.org/10.1016/j.nantod.2022.101438

In-situ synthesizing carbon nanotubes on cement to develop self-sensing cementitious composites for smart high-speed rail infrastructures

Siqi Ding [1], Yu Xiang [2], Yi-Qing Ni [2,3], Vijay Kumar Thakur [4,5],

Xinyue Wang [6], Baoguo Han [6*], Jinping Ou [1]

[1] School of Civil and Environmental Engineering, Harbin Institute of Technology, Shenzhen, Shenzhen 518055 China

[2] Department of Civil and Environmental Engineering, The Hong Kong Polytechnic University, Hung Hom, Kowloon, Hong Kong S.A.R.

[3] National Rail Transit Electrification and Automation Engineering Technology Research Center (Hong Kong Branch), Hung Hom, Kowloon, Hong Kong S.A.R.

[4] Biorefining and Advanced Materials Research Center, SRUC, Kings Buildings, Edinburgh, EH9 3JG, UK

[5] School of Engineering, University of Petroleum & Energy Studies (UPES), Dehradun 248007, Uttarakhand, India

[6] School of Civil Engineering, Dalian University of Technology, Dalian 116024, China

[*]Corresponding author: hanbaoguo@dlut.edu.cn; hithanbaoguo@163.com

Abstract

Self-sensing cementitious composites (SSCCs) with carbon nanotubes (CNTs) have attracted extensive attention because of their excellent mechanical and durability properties combined with multifunctional benefits. However, their performance modulation, as well as scalable manufacturing and application, are limited by the uniform dispersion of CNTs inside them. Here, a straightforward approach to *in-situ* synthesizing CNTs on cement (CNT@Cem) toward alleviating the CNTs' dispersion issue and enhancing their composite efficiency and effectiveness is explored. Due to the inherently containing silicate and ferrite phases, microscale cement particles act as effective substrate-bound catalysts, facilitating high-yield and strongly anchored CNTs growth. The hierarchically structured CNT@Cem integrates the dual functions of reinforcement and conduction, significantly affecting early-age hydration, mechanical, electrical, and self-sensing properties of the final SSCCs with CNT@Cem. The CNT@Cem structure can promote early-age hydration while slowing the later hydration rate and hindering the strength development of the SSCCs. The addition of CNT@Cem can be effective in tailoring the electrical microstructures to enhance the electrical conductivity and self-sensing sensitivity of the SSCCs.

The SSCCs with CNT@Cem achieved a maximum stress sensitivity of 2.87 %/MPa with a gauge factor of 748. They demonstrated excellent repeatability and stability, outstanding adaptability to various applied conditions, and fast response and recovery. The developed SSCCs-engineered smart track slab is competent in axle counting and speed detection. It opens up a new territory to develop high-performance and versatile SSCCs-engineered smart components/structures for long-term, wide distribution, and low-cost monitoring of high-speed rail (HSR) infrastructures.

Keywords: Self-sensing; carbon nanotube/cement; *in-situ* synthesis; cementitious composites; smart high-speed rail infrastructures.

1. Introduction

Over the past decades, the massive high-speed rail (HSR) infrastructure development has effectively alleviated the traffic burden and fostered coordinated regional economic growth. Still, it has also raised growing safety concerns. With safety being a paramount priority in rail transportation, tremendous efforts have been spent on infrastructure health monitoring in HSR systems. Current sensing technologies for onboard and online monitoring of HSR systems from vehicles to HSR infrastructures mainly involve video supervision, acoustic emission-based techniques, ultrasonic-based techniques, electromagnetic induction techniques, and optical fiber sensors, among others [1–3]. Although they are potent alternatives in addition to manual visual inspection, most of them are expensive and of poor long-term durability and compatibility with HSR infrastructures. The majority of them are mainly made of cementitious composites and suffer from frequent service loads and harsh environmental conditions. In this regard, intrinsic self-sensing cementitious composites (SSCCs) would be an appropriate supplement to the existing sensing technologies, allowing for long-term, wide distribution, and low-cost monitoring of HSR infrastructures.

As an emerging sensing technology, SSCCs, fabricated by adding conductive fillers into conventional cementitious materials, can sense their own conditions and changes in the surrounding environment by measuring the variation of electrical signals. Due to their cementitious nature, SSCCs feature inherent host compatibility and an identical lifespan with the construction materials. In addition, SSCCs can be directly used as a load-bearing component of concrete infrastructures because of their superior mechanical properties and durability [4–8]. The

past several decades have witnessed the broad engineering applications of SSCCs, such as strain sensing [9], damage detection and localization [10], structural modal identification [11], temperature sensing [12], and traffic detection [13]. The SSCCs have also exhibited great potential for monitoring railway concrete infrastructures [14]. For example, Lee et al. developed a wireless smart railway sleeper using SSCCs. However, the SSCCs-based railway sleeper has yet to be applied for real-time monitoring of HSR infrastructure [15].

To meet the high demand for SSCCs within the HSR field, next-generation SSCCs should have the merits of high sensitivity, excellent repeatability, extensive dynamic range, fast response and recovery time, and scalable manufacturing. As the functional agent, conductive fillers, mainly including carbon-based and metallic materials, determine the sensing performance of the resulting SSCCs [16]. Nano carbons, in particular carbon nanotubes (CNTs), which possess unique structures and combined superior mechanical and electrical properties, are regarded as one of the most promising conductive fillers for constructing SSCCs [17–22]. However, a critical factor determining the properties of SSCCs is the uniform dispersion of CNTs inside them. Due to the high aspect ratio and specific surface energy, and the van der Waals force, CNTs agglomerate too easily in the matrix, leading to the formation of defective sites inside the composite and compromised CNTs' filler efficiency [23,24]. Furthermore, non-uniformly distributed CNTs cannot form stable and continuous conductive networks within the matrix, resulting in poor sensing performance in terms of sensitivity and repeatability [25]. Chemical modifications of CNTs combined with mechanical dispersion methods are often suggested to create a satisfactory dispersion [24]. However, mechanical dispersion methods such as ultrasonication have low dispersion efficiency and damage CNT structures. The re-agglomeration of CNTs in pore solution is often found after the removal of ultrasonication [26]. Covalent functionalization of CNTs via the introduction of functional groups can reduce the van der Waals interaction between CNT bundles and generate electrostatic repulsion between the charged CNTs, thus improving the CNTs dispersion [27]. However, covalent functionalization of CNTs involving aggressive processes may introduce structural defects and break CNTs, detrimental to the electrical and mechanical properties of CNTs [28]. Non-covalent modification of CNTs via surfactants adsorption and polymers wrapping [29] can block the connectivity and conductivity of CNTs network, entrap air in the cement paste and impede cement hydration [30]. These complicated,

multi-step dispersion methods restrict CNT's large-scale applications in many fields.

Recent advances in nano-synthetic and nanocomposite technologies offer new strategies such as *in-situ* chemical vapor deposition (CVD), electroless deposition, microwave irradiation, and electrostatic self-assembly for developing a new class of CNT-based hierarchical fillers through the direct growth/graft of CNTs on microscale fillers such as carbon fibers and cement particles, to deal with the dispersion issue of CNTs by transferring the nanoscale dispersion into the microdomain as well as improving their composite effectiveness and efficiency [30–36]. Among these strategies, the *in-situ* CVD-grown CNTs on cement particles (CNT@Cem) are more versatile, tunable, straightforward, and scalable, enabling the synthesis and dispersion of CNTs in one step. On the one hand, the morphology, structure, distribution, and interface of CNTs on cement particles can be well mediated by varying CVD parameters such as carbon source, catalyst, gas composition, feeding rate, growth temperature, and time to fulfill various applications scenarios [37]. On the other hand, this strategy can eliminate any ultrasonication and functionalization steps, retaining the integrity of CNT structures and properties and optimizing the performance retention of CNTs in cement matrices [32]. The hierarchically structured CNT@Cem composites can act both as functional fillers and as matrix materials themselves directly involved in the hydration and hardening processes of the SSCCs. The production of the CNT@Cem is also expected to be integrated into the cement production process to realize the low-cost, low-carbon, and industrialized manufacturing [38]. However, investigations on the synthesis of such unique nanostructure are limited and have mainly concentrated on the CVD process's parametric studies [38–43]. Nasibulin et al. first explored the feasibility of using the CVD method to grow CNTs directly on the surface of cement particles. They found that this method was highly efficient for the low-temperature and high-yield synthesis of CNTs[38]. CNTs have also been successfully grown on silica fume, fly ash, sand, and soil using the CVD method [44]. Ghaharpour et al. studied the effect of synthesis parameters on the yield and morphology of the grown CNTs and found that the average diameter and yield of CNTs increased with reaction temperature, synthesis time, and catalysts contents [40]. No study has looked at the effect of CNT@Cem on cement hydration and properties of the resulting cementitious composites, particularly the self-sensing properties of SSCCs with CNT@Cem.

Because of the enormous potential applications of SSCCs with CNT@Cem in HSR

120 infrastructure, herein, we report a straightforward method for scalable fabrication of next-
121 generation SSCCs with high conductivity and robust self-sensing performance, and extent their
122 application as a monitoring system integrated with an SSCCs-engineered smart track slab for
123 HSR train monitoring. We perform a detailed effort to synthesize hierarchically structured
124 CNT@Cem composite filler by growing CNTs on cement particles via the *in-situ* CVD method.
125 The as-synthesized CNT@Cem possesses a unique nest-like morphology with strong interfacial
126 bonding between the CNTs and the cement particles, which would be beneficial to the
127 reinforcement of mechanical properties of CNT@Cem/cement composites and avoid re-
128 agglomeration of CNTs in cement pastes. Crucially, the inclusion of CNT@Cem would
129 effectively tailor the electrical microstructures, enhancing the electrical conductivity and self-
130 sensing sensitivity of the SSCCs. In this paper, the SSCCs with CNT@Cem demonstrate a gauge
131 factor as high as 748, which outperforms most of the SSCCs reported previously. The distinctive
132 properties and functionalities compatible with the large-scale and sustainable manufacturing of
133 the SSCCs allow their potential applications for long-term, wide distribution, and low-cost
134 monitoring of HSR infrastructures.

135 ## 2. Experimental section

136 ### 2.1. *Synthesis of CNT@Cem via CVD*

137 Portland cement (PC, CEM I 52.5, BS EN197-1:2000) and nano-Al_2O_3 (99.99%, γ-phase, 20
138 nm, Aladdin) with a mixing ratio of 100:4 were introduced into $Ni(NO_3)_3 \cdot 9H_2O$ isopropanol
139 solution. The mixture was magnetically stirred, oven-dried, and calcinated to obtain Ni-Al-
140 Cement (NAC) catalyst, precursor. The NAC catalysts were heated at a rate of 10 °C/min to
141 desired growth temperatures in a CVD system under a gas mixture of $C_2H_2/H_2/N_2$ for different
142 growth time. After this, the sample was allowed to cool down to room temperature under N_2
143 (detailed synthesis process and chemical compositions of the catalyst precursor and CNT@Cem
144 are shown in Experimental Procedures and **Table S1** in the Supporting Information).

145 ### 2.2. *Preparation of SSCCs with CNT@Cem*

146 The raw materials used for the preparation of SSCC specimens include as-received

CNT@Cem, raw PC (CEM I 52.5, Green Island Portland Cement Co., Ltd.), distilled water, silica fume (920D, Shanghai Tian Kai Silicon Fume Co. Ltd.), and polycarboxylate superplasticizer (ViscoCrete 3301E, Sika Ltd.). The mixture proportions are presented in **Table S2**, in which the amounts of water, silica fume, and superplasticizer were by mass of cement, composed of PC and CNT@Cem. The water to cement ratio of each mixture was kept constant at 0.4. First, the pre-weighed CNT@Cem powders were dry-mixed with silica fume and raw PC using a mechanical stirrer (MXF-C, Shanghai Muxuan Industrial Co., Ltd.) at a low speed for 2 min. The polycarboxylate superplasticizer was diluted with water and then gradually added to the dry mixture in three divided times, with 30 s of low-speed stirring followed by 2-min high-speed stirring. The well-stirred mixtures were then cast in oiled steel molds (20 mm × 20 mm × 20 mm), and two copper electrodes were inserted in each mixture with an interval of 10 mm. An electric vibrator was used for mixture compaction. After 24-hour placement in an environmental chamber (20 ±0.5 ℃ and 98% relative humidity), all specimens were demolded and transferred into a lime-saturated curing tank at room temperature for 27 days.

2.3. ***Characterization***

Field emission scanning electron microscopy (FESEM, Hitachi SU8020, Japan) at an operating voltage of 5 kV and transmission electron microscope (JEOL 2100F, Japan) at an operating voltage of 200 kV was used to characterize the morphologies of CNT@Cem. Energy-dispersive X-ray spectroscopy (EDX) analysis was performed to determine the elemental maps of the CNT@Cem. The amount of CNTs deposited on CNT@Cem was determined by thermogravimetric analysis (TGA, Mettler-Toledo TGA/DSC3+, Switzerland), in which the sample was heated to 900 ℃ under air atmosphere (23% oxygen) at a rate of 10 ℃/min. The crystalline structure of CNTs was evaluated using a Raman spectroscopy (Renishaw 2000, Britain) equipped with a 632.8 nm helium-neon laser. The phase compositions of PC and CNT@Cem were determined by X-ray diffraction (XRD) measurement (Bruker D8 Advance, USA) with CuKα radiation operated at 40 kV and 40 mA. XRD patterns were collected in the 2θ range of 5-80° with a step width of 0.02° and a step time of 1.0 s. The mineral compositions were analyzed using quantitative XRD (QXRD, Rietveld refinement, TOPAS). The Brunauer-Emmett-Teller (BET, Micromeritics Tristar ASAP 2020HD88, USA) specific surface area was measured

by N_2 adsorption measurements at about 77 K. The density of the CNT@Cem was measured using a true density tester (JWGB JW-M100A, China) at 30 ℃ and 0.1 kPa.

To determine the hydration phases of the SSCCs with CNT@Cem, TGA measurements with a heating rate of 10 ℃/min up to 1000℃ under N_2 atmosphere and XRD measurements with the same setting for CNT@Cem were performed. Before the testing ages of 1, 7, and 28 days, the hydration of the ground sample was stopped by solvent exchange using isopropanol and then in acetone for the 20s. Afterward, the samples were washed with isopropanol and stored in a vacuum desiccator until further testing. The hydration heat evolution of SSCCs with CNT@Cem was analyzed using an eight-channel isothermal calorimeter (TAM AIR TA, USA) under an isothermal condition of 25 ℃ for three days. 10 g of the pastes were mixed in a beaker using a glass rod for 2 minutes and then immediately placed into the calorimeter. The microstructure of the SSCCs with CNT@Cem specimens after fracture was observed using a FESEM (Tescan MAIA3, Czech). The compressive strength of the SSCCs with CNT@Cem specimens was tested using a hydraulic material testing system (MTS810-50kN, MTS, USA) equipped with an auto-alignment MTS compression platen (Model 643.06) at a constant loading rate of 1.2 mm/min. Two longitudinal strain gauges were symmetrically deployed on a pair of opposite sides of each specimen, and a dynamic data logger (DC-204R, TML, Japan) was used for strain measurement.

As to the electrical properties of the SSCCs with CNT@Cem, the direct current (DC) electrical resistance of the unloaded SSCCs with CNT@Cem was measured by a two-probe method using a digital multimeter (DMM7510, Keithley Instruments Inc., USA). Each specimen's electrical resistance was calculated by taking the average of three data collected after 2 h to mitigate any shift due to the polarization effect.

The self-sensing properties of the SSCCs with CNT@Cem were performed under repeated compression using the MTS810 machine. To investigate the self-sensing properties of SSCCs with CNT@Cem, experiments were first conducted under monotonic uniaxial compression to 25 MPa at a loading rate of 1.2 mm/min. Prior to the tests, all samples were connected to the ends of the multimeter for 2 h to minimize the polarization effect on resistance variations. The specimens were separated from the compression platens by thin insulating plates to avoid electrical interference. The compressive force, strain, and electrical resistance were simultaneously collected at a sampling rate of 10 Hz during the loading process. All experiments were conducted

at room temperature.

To devise a monitoring system integrated with an SSCCs-engineered smart track slab, the SSCCs connected with two shielded cables were directly embedded into the track slab of a CRTS-II slab ballastless track and then encapsulated with rapid hardening polymer-based cement mortar (PCM-II, China Academy of Railway Science). The electrical resistance change was converted into a voltage signal by connecting the sensor with a reference resistor (1000 Ω) for voltage sharing. The circuit was powered with a 1.5 V battery. The voltage signal was collected using a data acquisition system consisting of a portable data acquisition card (NI USB-6009, National Instruments Corporation, USA) and a computer with a sampling rate of 10 kHz. Note that the tests were conducted during a maintenance window so that the trains were passed over at a lower speed than the maximum speeds during commercial operation.

3. Results and discussion

3.1. Morphology and structure of CNT@Cem

The synthesis process of CNT@Cem, including catalyst impregnation, calcination, and CVD growth, is schematically illustrated in **Figure 1**a. Briefly, PC and nano-Al_2O_3 was introduced into $Ni(NO_3)_3 \cdot 9H_2O$ isopropanol solution, followed by magnetically stirring. The suspension was then calcinated to obtain Ni-Al-Cement (NAC) catalyst precursor for CVD treatment. Due to the doping of the green $Ni(NO_3)_3 \cdot 9H_2O$ catalyst, the color of cement particles changed from grey to grey-green (**Figures 1**b-e). After calcination at 400 ℃ for 12 h, the color became brown-black since the $Ni(NO_3)_3 \cdot 9H_2O$ was thermally decomposed into brown-black Ni_2O_3 (**Figure 1**d) [45] and then turned dark-black after CVD treatment, indicating the successful deposition of CNTs (**Figure 1**e). During heat treatment, the thermal decomposition of gypsum ($CaSO_4 \cdot 2H_2O$) in cement particles did not affect appearance change. The SEM observations (**Figures 1**e-h) revealed that Ni-catalyst nanoparticles were uniformly deposited on the surface of cement particles, thus causing appearance variations. The chemical composition identified by EDX analysis shows that the amount of Fe on the raw PC surface was 2.82 wt.% (**Figure 1**f), and no Ni element was identified, in agreement with the X-ray fluorescence (XRF) data (**Table S1**). After catalyst impregnation (**Figure 1**g) and calcination (**Figure 1**h), the high amount of Ni

234 detected confirmed the presence of catalyst particles on cement surfaces to provide templates for
235 CNT growth. **Figure 1**i shows a uniform and good coverage of CNTs on cement particles with
236 lengths of several micrometers under a CVD condition of $C_2H_2/H_2/N_2$=40/40/100 sccm, 550 ℃,
237 20 min.
238

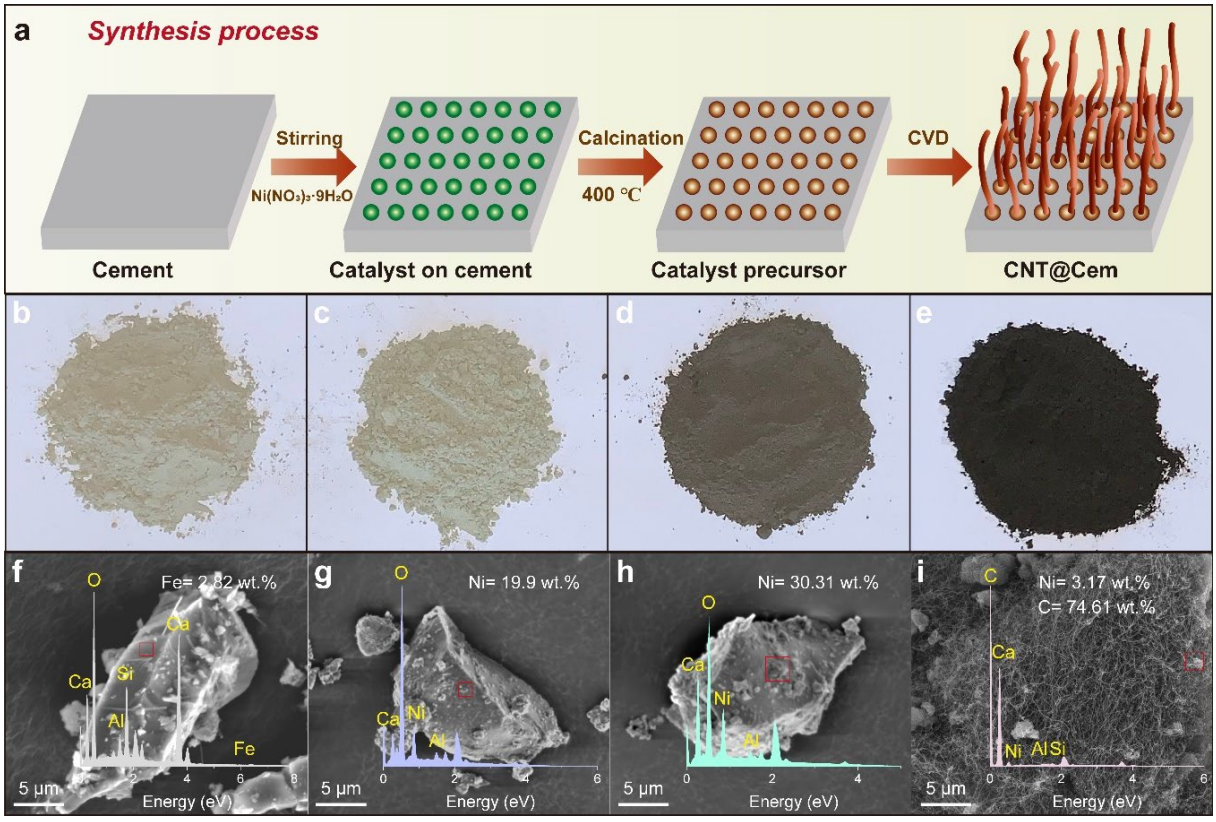

Figure 1. Synthesis of CNT@Cem via CVD method. (a) Schematic illustration of the synthesis process. The appearance of (a) PC particles. (b) CNT@Cem catalyst precursor after drying. (c) CNT@Cem catalyst precursor after calcination. (d) the as-grown CNT@Cem. SEM images and EDX spectra (Insets) (e) Raw PC particles. (f) CNT@Cem catalyst precursor after drying. (g) CNT@Cem catalyst precursor after calcination. (h) the as-grown CNT@Cem. Growth condition: $C_2H_2/H_2/N_2$=40/40/100 sccm, 550 ℃, 20 min.

239

240 To validate the interfacial bond between the CNTs and the cement particles, the as-grown
241 CNT@Cem was sonicated in isopropanol using an ultrasonic cleaner (Crest, 45 kHz) for 30 min.
242 As shown in **Figure 2**a, the CNTs were firmly adhered to the cement surface without obvious
243 fall-offs, supported by the lack of obvious change in the isopropanol solution before and after
244 sonication (**Figure 2**a, inset). In contrast, the CNTs formed cross-linked networks and generated
245 a bridging effect between cement particles (**Figure 2**b), which would be beneficial to the

246 mechanical properties of CNT@Cem/cement composites [44], and avoid re-agglomeration of
247 CNTs in cement pastes [46]. The high-magnification SEM image of the CNT@Cem demonstrated
248 CNT's outer diameter mainly ranging from 25-55 nm, indicating the as-formed CNTs were
249 multi-walled (**Figure 2**c). The High-Angle Annular Dark Field scanning TEM (HAADF-STEM)
250 image and the corresponding elemental mapping images demonstrated the distribution of C, Ni,
251 Fe, Ca, O, and Al elements on the as-grown CNT@Cem. As observed, Ni elements were
252 homogeneously distributed in CNTs and separated from Ca, O, Al, and Fe elements associated
253 with cement particles (**Figure 2**d), suggesting the tip-based growth mechanism of the CNTs on
254 cement. Further evidence was given by TEM observation that Ni-catalyst nanoparticles were
255 observed among the CNTs, and the CNTs were synthesized into the cement particles in situ with
256 a vertical growth (**Figure 2**e). This is an essential feature of CNT@Cem in terms of strong
257 interfacial bonding between the CNTs and the cement matrix. The ring-like pattern in selected
258 area electron diffraction (SAED) in **Figure 2**e shows the (002) and (004) diffraction rings of
259 CNTs. Additionally, the HRTEM result shows the as-grown CNTs with Ni catalyst at the end
260 were multi-walled while poorly crystallized with an outer diameter of 31.5 nm, consistent with
261 the SEM results (**Figures 2**f, g). The apparent lattice fringes have a neighboring spacing of 0.34
262 nm corresponding to graphite's (002) plane. The detailed structure of the Ni-catalyst
263 nanoparticles during the growth process demonstrates lattice fringes with a periodicity of ~0.2
264 nm corresponding to the (111) planes in Ni (**Figure 2**g). The active Ni surface provides sites for
265 the nucleation and growth of graphene layers of the CNTs [48,49].
266

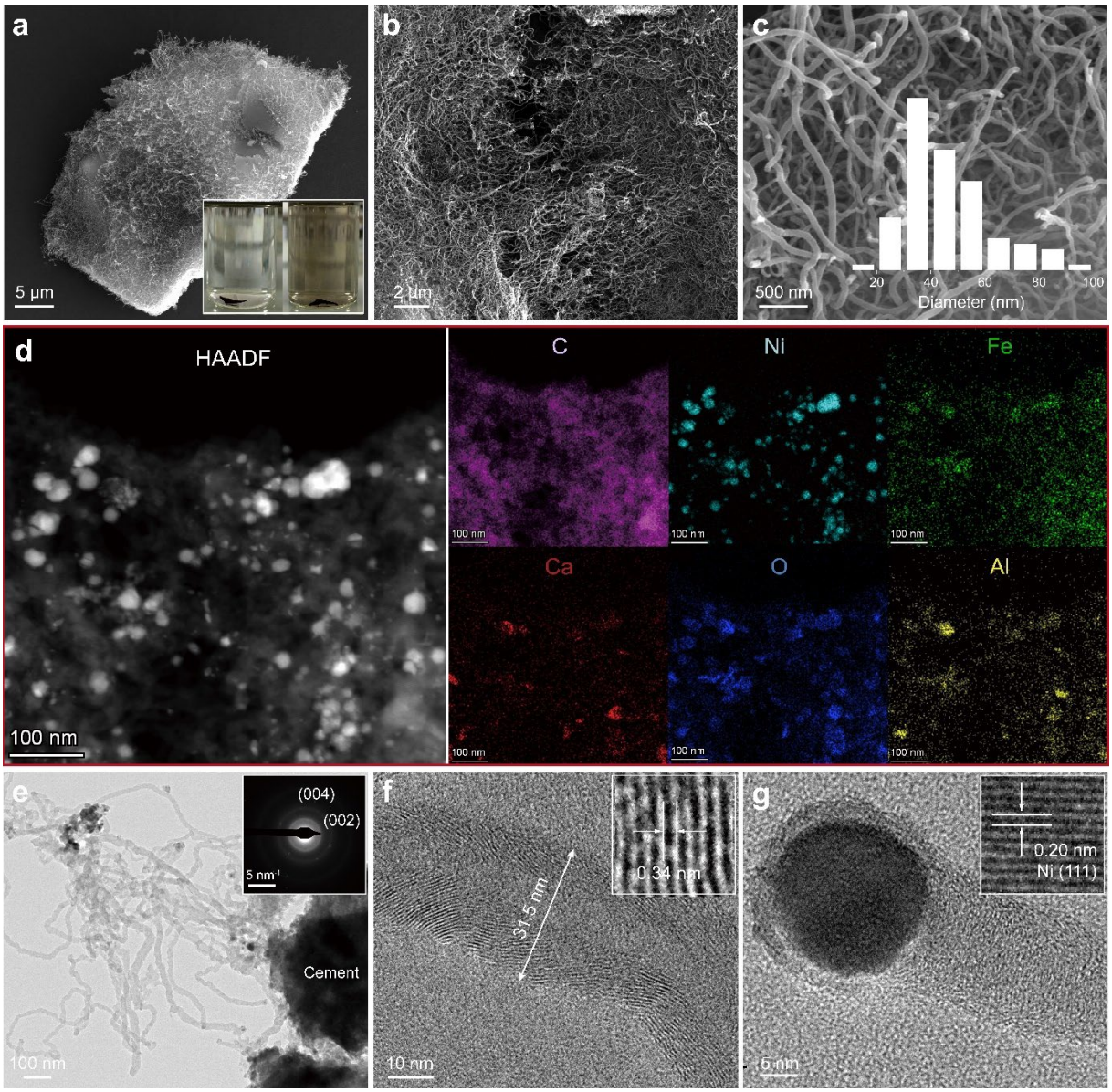

Figure 2. Morphology of CNT@Cem. (a) and (b) SEM images of the as-synthesized CNT@Cem after 30 min sonication. Inset in (a) shows the as-grown CNT@Cem before and after sonication. (c) High-magnification SEM image of the CNT@Cem after sonication. Inset shows the diameter distribution. (d) HAADF-STEM image and the corresponding elemental mapping images of the CNT@Cem. (e) TEM image of the CNT@Cem after sonication. Inset shows the selected area electron diffraction (SAED) pattern. (f) HRTEM image of CNTs. (g) HRTEM image of Ni nanoparticle encapsulated in CNTs. Growth condition: $C_2H_2/H_2/N_2$=40/40/100 sccm, 550 ℃, 20 min.

3.2. Effect of temperature on CNT@Cem growth

The effect of temperature on CNT@Cem growth under a temperature range of 450 - 850 ℃

with an interval of 100 ℃ was explored. As shown in **Figures 3**a-f, due to the high catalytic activity of Ni species at low temperature, short and entangled CNTs were readily formed with good coverage on the cement surface in the 450 ℃ sample, which is different from previous works in which no carbon deposits were observed below 550 ℃ when using Fe species as catalysts [41]. For CNT@Cem samples grown at 550 ℃ and 650 ℃, the length of CNTs rapidly increased and the average CNT diameter increasing with synthesis temperature is visible. Up to 750 ℃, the CNT feature was no longer well-defined, forming enormous quantities of graphite or coke. The BET surface areas of the CNT@Cem samples synthesized at different temperatures all significantly increased concerning the raw cement after the deposition of carbon materials (**Figure 3**g). The maximum BET surface area was found to be 45.69 m^2/g for the 550 ℃ sample, which agrees with the SEM result that the 550 ℃ sample had the most abundant CNTs.

The temperature-dependent CNT growth was also evidenced by XRD analysis (**Figure 3**h), with the peak at $2\theta = 26^{o}$ (indexed as C(002)) corresponding to the interplanar spacing of 0.34 nm of the CNTs visible in the case of 450 - 650 ℃ while vanishing for the 750 ℃ and 850 ℃ samples. The XRD spectra also observed the phase transitions of PC and CNT@Cem samples synthesized at different temperatures. The peak at $2\theta = 11.7^{o}$ assigned to gypsum ($CaSO_4 \cdot 2H_2O$) vanished due to its thermal decomposition after calcination and CVD process, transiting into anhydrite ($CaSO_4$, peak at $2\theta = 25.5^{o}$), which is also indicated in the Raman spectrum (**Figure 3**i) where the Raman band of gypsum (1010 cm^{-1}) disappeared. Moreover, the peak intensities decreased with the increasing temperature due to the further decomposition of anhydrite at high temperatures. The most significant change is that the peak intensity of (Fe, Ni)C solid solution ($2\theta = 45^{o}$) was enhanced with the increasing temperature [50]. The peak of C_4AF was disappeared at 850 ℃, indicating the strong interactions among Ni, Fe, and C species [51]. This could be one of the reasons for the reduced CNTs at high temperatures, as the formation of metallic carbide causes the catalyst deactivation [52–54].

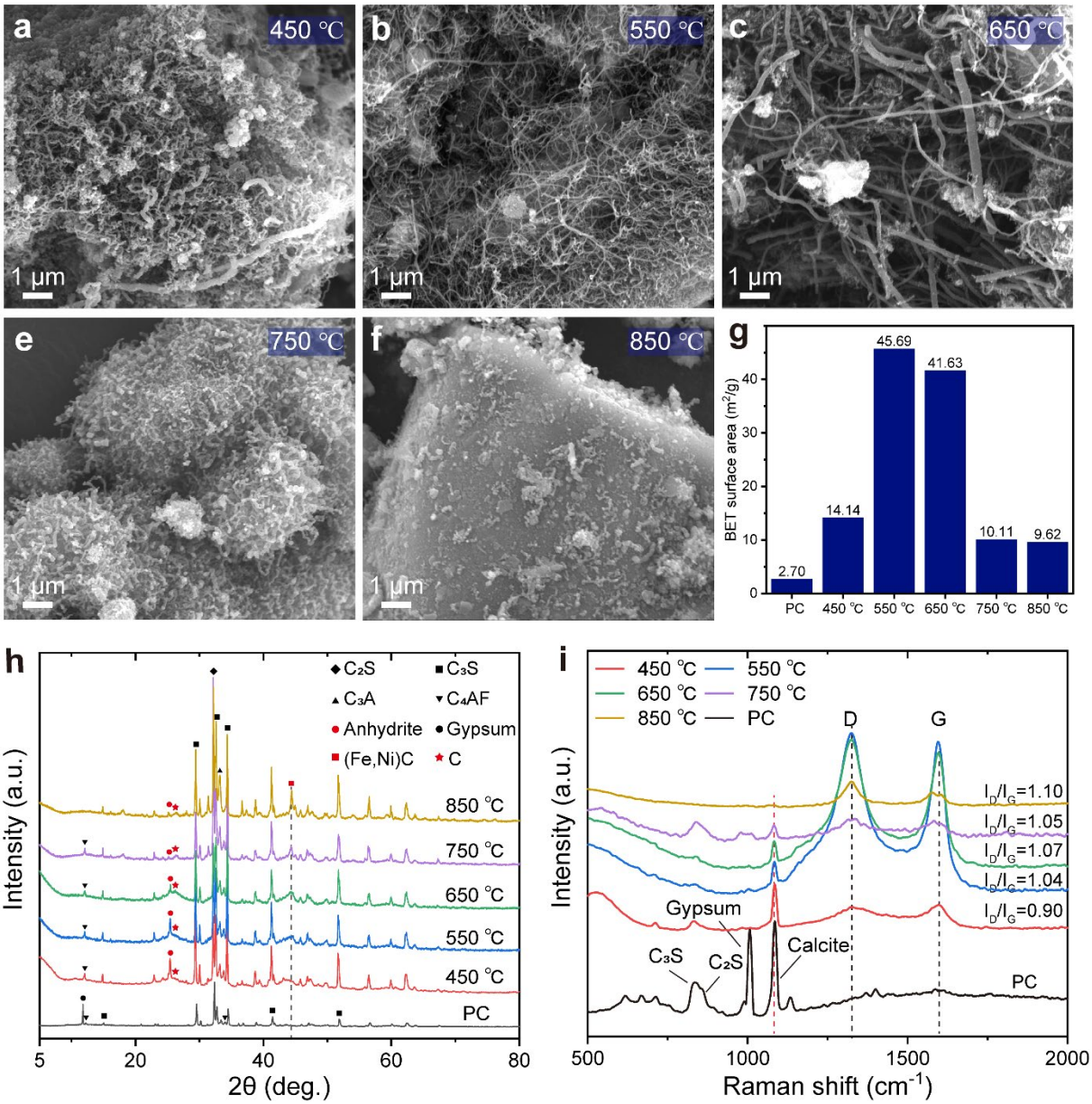

Figure 3. Effect of temperature on CNT@Cem growth. SEM images of CNT@Cem grown at (a) 450 °C. (b) 550 °C. (c) 650 °C. (d) 750 °C and (e) 850 °C. (g) BET surface areas of raw cement and the CNT@Cem grown at different temperatures. (h) XRD analysis of phase evolutions of the CNT@Cem grown at different temperatures. (i) Raman spectra of raw cement and the CNT@Cem grown at different temperatures. Growth condition: $C_2H_2/H_2/N_2$=40/40/100 sccm, 20 min.

The comparable I_D/I_G values of all CNT@Cem samples within the range of 0.9 - 1.1 are lower than the commercial CNTs (I_D/I_G = 0.68) [33], indicating the formation of poorly crystallized CNTs associated with a large number of defects. In the Raman spectrum of the PC,

C_3S at 828 cm^{-1}, C_2S at 864 cm^{-1}, gypsum at 1010 cm^{-1} and $CaCO_3$ at 1086 cm^{-1} were detected [55–57]. The intensity of $CaCO_3$ at 1086 cm^{-1} gradually attenuated with increasing temperature and completely disappeared at 850 °C, indicating that $CaCO_3$ was completely decomposed under this CVD condition. The decomposition of $CaCO_3$ leads to the release of CO_2 as an etching agent that results in the deactivation of the catalyst particles for CNT synthesis at such a high temperature [38]. In addition, the C_2H_2 decomposition is extremely fast at high temperatures, resulting in the total amount of carbon deposited on the catalyst exceeding the catalyst solubility, forming encapsulating coke on the catalyst (**Figure 3**f). The high temperature would also facilitate the mobility of Ni catalyst particles, thus forming too large Ni agglomerations for optimum CNT growth [40,58]. This may be another reason for the reduced CNT synthesis at high temperatures. Conclusively, the most acceptable temperature range for the CNT@Cem growth was 550-650 °C, as revealed in this study.

3.3. Evolution of CNT@Cem with reaction time

Figures 4a-d show the SEM results of the CNT@Cem samples grown for different reaction time. As shown in **Figure 4**a, only nano-sized carbon dots were formed on the catalyst, which would act as seeds for sustainable CNT growth. With increasing reaction time, the density of the CNTs and size of the CNT@Cem increased remarkably. The initially vertical growth direction of CNTs became irregular due to different growth rates and the restriction of dense CNT coverage, forming a nest-like morphology of CNT@Cem after 30 min (**Figure 4**d). TG-DTG analysis was performed in an air atmosphere to estimate the growth rate of CNTs. As shown in **Figures 4**e, f, the PC demonstrates three DTG peaks at around 120 °C, 440 °C, and 700 °C, corresponding to the dehydration of $CaSO_4{\cdot}2H_2O$, decomposition of $CaSO_4$ and decarbonation of $CaCO_3$ [59]. In comparison, a temperature range of 480 - 550 °C attributed to the decomposition of CNTs and a $CaCO_3$ decomposition peak at around 700 °C were observed in the DTG curves of the CNT@Cem samples. The prolonged growth time caused an increase in the decomposition temperature of CNT, indicating a higher level of crystallinity. While no peaks at around 120 °C and 440 °C were observed in the CNT@Cem samples as the gypsum and anhydrite were decomposed after the CVD process, which was validated by the XRD (**Figure 3**h) and Raman characterizations (**Figure 3**i).

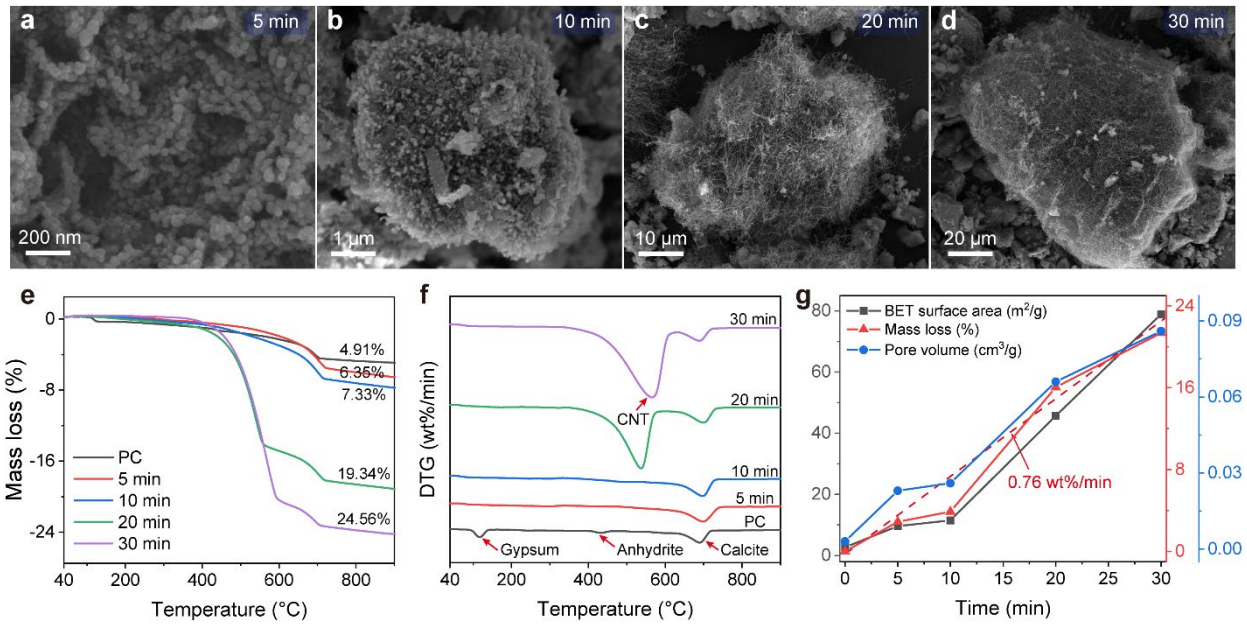

Figure 4. SEM images of CNT@Cem grown for (a) 5 min. (b) 10 min. (c) 20 min. (d) 30 min. (e) TG analysis. (f) DTG analysis of CNT@Cem grown for different reaction time. (g) Mass losses derived from TG curves, BET surface areas, and pore volumes of CNT@Cem grown as a function of reaction time. Growth condition: $C_2H_2/H_2/N_2$=40/40/100 sccm, 550 °C.

Figure 4g presents the mass loss accounting for the CNT decomposition of each sample. Using linear regression, a mass loss rate of 0.76 wt.%/min was obtained. The BET surface areas and pore volumes of the CNT@Cem samples showed a similar trend as the TG-DTG results. The 30-min sample has a BET surface area as high as 78.89 m^2/g (30 times higher than the raw cement of 2.7 m^2/g) and pore volume of 0.086 cm^3/g (28 times higher than the raw cement of 0.003 cm^3/g) due to the decoration of CNT forests. In fact, CNT growth under certain CVD conditions is unable to proceed indefinitely. Slowing or even cessation of CNT growth after a certain amount of time has been previously reported in CNT grown on other substrates such as silica powder [60], alkaline earth carbonate [61], and quartz plates [62] due to catalyst encapsulation or deactivation. The fact that CNTs grow continuously for 30 min in this study indicates that the nickel catalyst particles remain catalytically active on this long reaction time.

3.4. Properties of CNT@Cem engineered SSCCs

As discussed above, the nest-like CNT@Cem has dense and long CNTs covalently anchored to cement particles and has distinctive characteristics with raw cement such as enhanced specific

surface area and reduced gypsum and $CaCO_3$ contents. The replacement of cement by CNT@Cem is expected to affect the properties of CNT@Cem/cement composites and endows functionality. To investigate the utilization of the as-synthesized CNT@Cem hierarchical fillers in tailoring SSCC performance, a batch of CNT@Cem was afterward prepared using 100 mM $Ni(NO_3)_3 \cdot 9H_2O$ isopropanol solutions as catalyst precursors with a CVD regime of $C_2H_2/H_2/N_2$=40/40/100 sccm at 550 °C for 30 min, based on a criterion of growing CNTs with high density and long length. Then, the SSCC specimens, including as-received CNT@Cem, raw PC, water, silica fume, and polycarboxylate superplasticizer, were prepared according to the mixture proportions presented in **Table S2.**

3.4.1. Hydration

The hydration heat evolution of the SSCCs with different contents of CNT@Cem for a period of up to 60 hours is shown in **Figure 5**. The addition of CNT@Cem did not cause a significant change in the hydration process of the SSCC blends, which can be divided into five stages, i.e., initial period (I), induction period (II), acceleration period (III), deceleration or retardation period (IV) and steady period (V) (**Figure 5**a) [63]. Due to superficial reactions of tricalcium aluminate (C_3A), the initial period occurred within just a few minutes. No apparent difference between the control (labeled as CNT@Cem-0) and the SSCCs with CNT@Cem was observed in such a short period. For the induction period, in comparison with the control, the addition of CNT@Cem shortened the induction period. It brought forward the onset of the acceleration period, which is consistent with the observations made by Makar et al. [64] and Li et al. [65]. The end of the acceleration period was also significantly hastened. **Figure 5**b shows that the age at peak heat flow indicated the final set decreased with increasing CNT@Cem content. The maximum peak shift was observed in the CNT@Cem-20 composite as 6.21 h, which is 50.12 % earlier compared with the control (12.45 h). As the acceleration period is mainly determined by the hydration of tricalcium silicate (C_3S), the observed change in hydration behaviors is attributed to the interaction between CNTs and C_3S hydration products (e.g., C-S-H gel and calcium hydroxide (CH)) [64]. The existence of CNTs on cement surfaces would provide nucleation sites for C-S-H and CH formation so that an increase of CNT@Cem significantly accelerated the SSCC hydration process [65–67]. Moreover, the reduced gypsum content in SSCCs would slow down the formation of ettringite that precipitates at the cement particle surface at an

early age, thus promoting the SSCC early-age hydration [63].

Figure 5c shows the total cumulative heat curves of the SSCCs with different contents of CNT@Cem up to 60 h. Except for the CNT@Cem-5 sample, the CNT@Cem samples basically have higher heats of hydration at the initial stages, falling below the control after 2.5 days. The slight increase in the heat of hydration at 2.5 days for the CNT@Cem-5 sample was found as 4 J g^{-1}. However, the cumulative heat release obviously reduced with increasing CNT@Cem content (**Figure 5**d). This is to be expected since the presence of CNTs on cement restricts the space available for hydration products growth. On the one hand, the CNTs can strongly wrap around cement surface and take up the nucleation sites, thus inhibiting the longitudinal growth of hydration products [64]. On the other hand, although the more nucleation sites can accelerate the hydration reactions at first, the extremely large specific surface area of CNTs would trap water molecules via electrostatic forces, in turn lowering the amount of water required to dissolve the anhydrous grains and complete the hydration in long-term evolution [68,69]. Therefore, the heat of hydration at later ages decreased due to the replacement of cement by CNT@Cem.

The TG-DTG results (**Figure S1**) for the SSCCs with CNT@Cem at ages of 1, 7, and 28 days agreed well with the thermal calorimetry that the CNT@Cem can promote the early-age hydration of cement while restricting the hydration rate at later ages, as evidenced by the overall mass loss of the control being much lower than the values measured for the CNT@Cem samples. As the curing age increased, the overall mass loss in the control caught up at 7 days and even overtook the CNT@Cem composites at 28 days. The peak intensity of C_3S in the XRD spectrum of the control (**Figure 5**e) was more remarkable than that of the CNT@Cem samples, indicating the lower hydration degree of the control at 1 day. The intensities of the main diffraction peaks of CH in the CNT@Cem composites increased with increasing curing ages while mirrored in the control, which is exactly consistent with the TG-DTG results. Similarly, the strongest peak intensity of CH in the CNT@Cem-5 sample followed the TG-DTG analysis that the CNT@Cem-5 had the largest mass loss due to the decomposition of CH. In addition, the CH formed in CNT@Cem composites had a preferred orientation to the (001) crystal plane, which always takes place in the porous zone where free space is available [70]. Except for the control, the mass loss associated with the decomposition of CH also increased with increasing hydration age, indicating the sustained formation of CH. The decrease of CH in control may be attributed to the

carbonation of CH into $CaCO_3$ and the consumption in "secondary pozzolanic reactions" with silica fume [59], as evidenced by increasing C-S-H and $CaCO_3$ peak areas in DTG curves. The CH content in the CNT@Cem composites was higher than that in control regardless of curing age, suggesting an improved formation of CH with the addition of CNT@Cem.

Both the XRD and TG-DTG results revealed that the CNT@Cem could increase the formation of CH at late ages, in contrast to previous studies that the addition of CNTs can reduce the size and crystal orientation of CH [71] or even have no effect on the formation of CH [66]. This phenomenon may be attributed to the nest-like CNT@Cem with a large surface area and a porous structure that would act as a "barrier" to prevent water from getting into the CNT@Cem hierarchical structure to reacting with the innermost cement. The structure in the vicinity of the CNT@Cem surface may be similar to the interfacial transition zone (ITZ) around aggregate, where preferentially oriented CH crystals are formed [72]. As evidenced by SEM observations (**Figure S2**), many unhydrated CNT@Cem particles existed in the composites after 28 days of curing, surrounded by abundant hexagonal plate-like CH phases can be found. Because the dense CNT forest on cement particles prevented water from reacting with the carpeted cement clinker, voids and CNTs not wrapped by hydration products were formed, which may have a negative impact on the final strength of the SSCCs. On the other hand, the incorporation of CNT@Cem provided CNTs reinforced C-S-H, CNT pull-out, and CNT bridging effects that would, in turn, enhance the mechanical properties of the SSCCs.

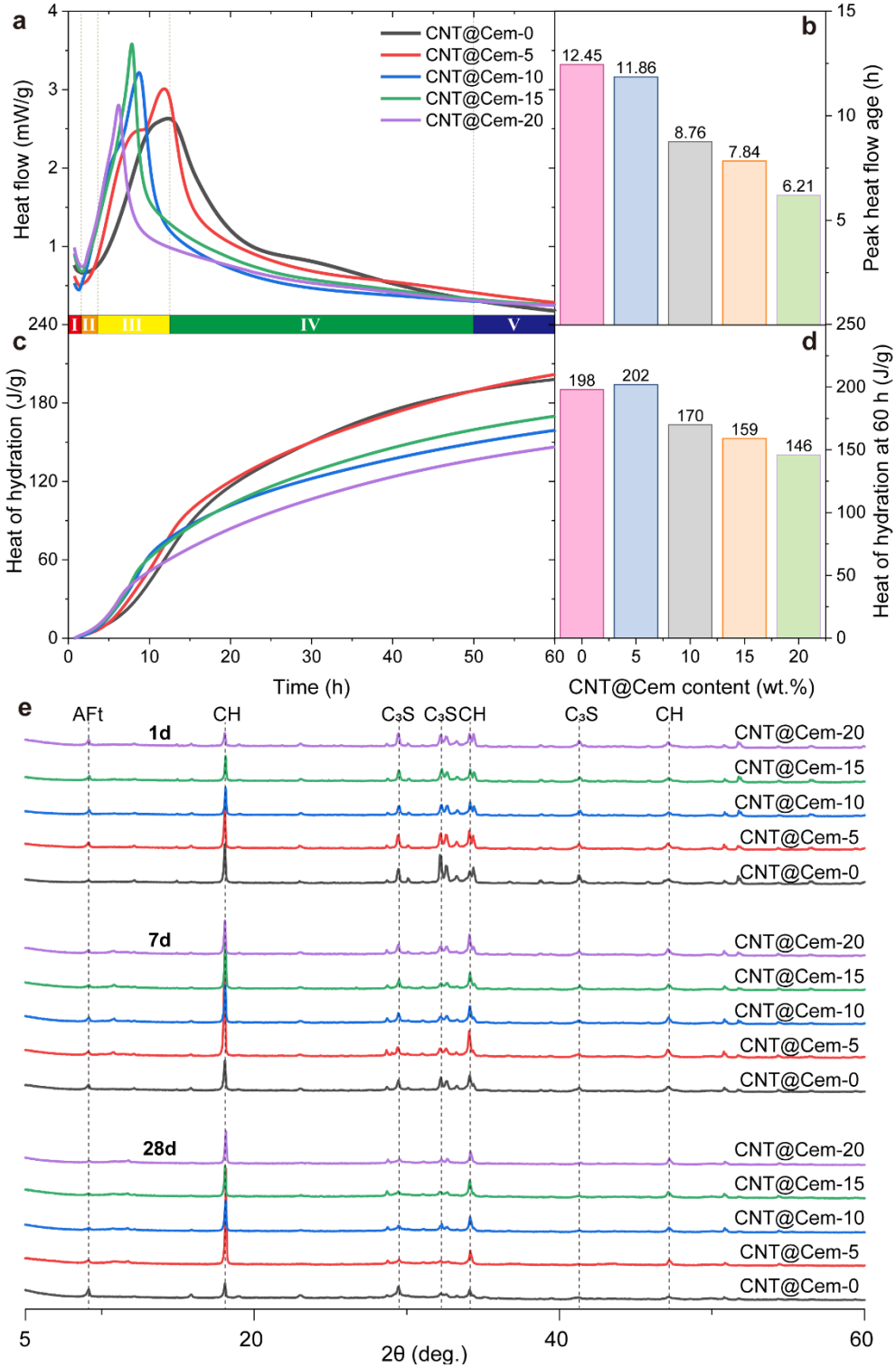

Figure 5. Calorimetric measurements of the SSCCs with CNT@Cem. (a) Heat flow. (b) Peak heat flow age. (c) Cumulative heat evolution. (d) The heat of hydration at 60 h. (e) XRD analysis of the SSCCs with CNT@Cem at 1, 7, and 28 days.

As shown in **Figure 6,** the compressive strength of the CNT@Cem-5 sample after 28 days was the highest. The increasing amount of CNT@Cem led to a decrease in the compressive stress at first-cracking (**Figure 6**a) despite a minor increase observed for the CNT@Cem-5 sample. Specifically, compared with the CNT@Cem-0 sample, the compressive strength increased by 3.1 MPa/3.9% for the CNT@Cem-5 sample and decreased by 12.8 MPa/16%, 24.1 MPa/30%, and 44.2 MPa/55% for CNT@Cem-10, CNT@Cem-15, and CNT@Cem-20 samples, respectively. Moreover, the addition of CNT@Cem negatively impacted Young's modulus (**Figure 6**b). However, it was observed from the compressive stress/strain curves that the addition of CNT@Cem led to a strain-hardening portion after the first peak due to the crack-bridging effect of CNTs [73]. The effect was more pronounced with the increasing CNT@Cem content. The decrease in the compressive strength of the SSCCs with the increasing amount of CNT@Cem may be attributed to three main mechanisms: (1) The increasing CNT@Cem incorporation in cement paste indicates a higher amount of water absorbed by CNTs, thus hampering cement paste hydration [74]; (2) The nest-like morphology of CNT@Cem leads to the excessive formation of highly oriented CH crystals around while reduces the amount of C-S-H gel, thereby less formation of hydration products that contribute to the strength of the composites [73,75]; and (3) The presence of voids and CNTs uncoated with hydration products may also be important factors for the compromised compressive strength of SSCCs with high contents of CNT@Cem.

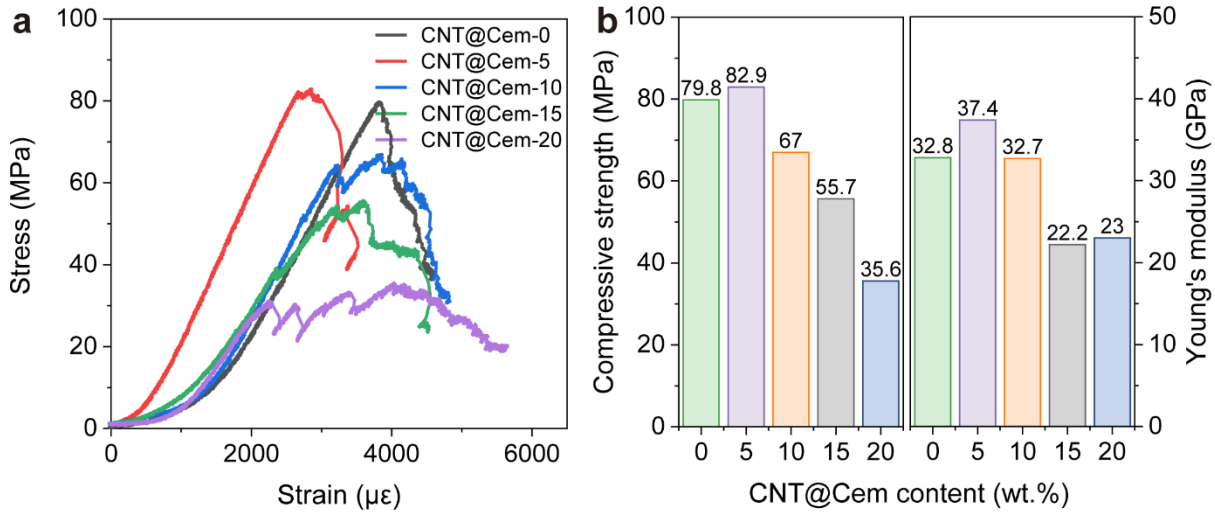

Figure 6. Effect of CNT@Cem on compressive properties of SSCCs with CNT@Cem after 28 days. (a) Relationship between compressive stress and strain. (b) Compressive strength and Young's modulus.

3.4.2. *Electrically conductive and self-sensing properties*

Due to the excellent conductive nature of CNTs, CNT@Cem is envisioned as an effective filler to enhance the electrical conductivity of the SSCCs, hence achieving self-sensing properties. **Figure 7**a shows the DC electrical resistances of the SSCCs with CNT@Cem as a function of filler content. A continuous decrease in the DC electrical resistance of SSCCs was observed with the increase of CNT@Cem content. As indicated in the log-log plot (**Figure 7**a, inset), the electrical resistance of the composites perfectly followed the principle of the percolation model. Percolation in the composites occurred when the filler content was near 5 wt.% (the pure CNT content is estimated to be 1.02 ± 0.06 wt.%), above which a rapid decrease in the DC electrical resistance took place from values of 2.94×10^5 Ω at 5 wt.% to 2.41×10^4 Ω at 10 wt.%. The percolation zone was almost the same as the SSCCs with commercial CNTs [34,76] and much lower than the CNT/NCB fillers [34,77] and multi-layered graphene [78]. Such an applausive percolation behavior was evidence of homogeneous dispersion of CNTs in the cementitious composites. An increase in CNT@Cem content above 10 wt.% produced a more gradual decrease in electrical resistance, with values of 2.76×10^3 Ω at 15 wt.% and 660 Ω at 20 wt.%. At CNT@Cem content as high as 25 wt.%, the electrical resistance can be as low as 350 Ω, which is approximately three orders of magnitude less than the control. At this time, the conductivity of the SSCCs is dominated by the CNT network of many connected paths through the cement matrix [4].

The relationship between compressive strain and the fractional change in electrical resistance (*FCR*) of the composites is presented in **Figure 7**b. The FCR of the control sample was nearly unaffected by the compression, indicating its poor strain/stress sensitivity. The CNT@Cem addition evidently enlarged the *FCR*, and such enhancement became more prominent as the CNT@Cem content increased, indicating a much higher sensitivity. The stress sensitivity was slightly increased from 0.11 %/MPa for CNT@Cem-0 to 0.29 %/MPa for CNT@Cem-5 (**Figure 7**c). When the CNT@Cem content increased to 10 wt.%, i.e., the percolation threshold, a remarkable increase in stress sensitivity was obtained as 1.82 %/MPa, which is 18 times higher than the control. This is consistent with the fact that the SSCCs with a filler content near the percolation threshold undergo an abrupt change of electrical resistance upon deformation, i.e., a high sensitivity [4]. Further increase of CNT@Cem content continuously increased the stress

sensitivity, achieving a maximum of 2.87 %/MPa for the CNT@Cem-25 sample. To obtain the gauge factor (|FCR|/ε, where ε is compressive strain), the linear parts of the plots (**Figure 7**b, within 300 με) were applied for the linear fitting. As shown in **Figure 7**c, the gauge factor of the control was determined as 21.5 and increased to 748 for the CNT@Cem-25 sample. The results indicated the extremely high sensitivity of the SSCCs with CNT@Cem under low levels of deformation. The gauge factor of the SSCCs with CNT@Cem-25 outperformed most of the SSCCs with commercial CNTs [17,79,80] as well as other reported conductive fillers including CB [81], CF [20], multi-layer graphene [78], CNT/TiO_2 [82], CNT/NCB [30, 83] and stainless steel wire [84], as demonstrated in **Figure 7**d.

In general, three mechanisms explaining the self-sensing behavior of the SSCCs with CNTs have been proposed [16]: (1) the change of intrinsic resistance of CNTs; (2) the change of contact resistance between CNTs due to the formation/breakage of CNT-CNT junctions; and (3) the change of tunnelling resistance due to the variations in the distance between adjacent CNTs. For the CNT@Cem-5 sample where filler content is below the percolation threshold, tunnelling conduction plays a key role in electrical conductivity, hence the decrease in tunnelling resistance under compression dominates the sensing mechanism. However, because of the strong bonding between the CNTs and the matrix and its high Young's modulus (**Figure 6**b), the sensitivity of the CNT@Cem-5 sample is not significantly enhanced compared to the control. When the CNT@Cem content reaches the percolation threshold, the abundant conductive paths formed by CNT@Cem increase the number of CNT-CNT junctions and the possibility of tunnelling conduction. In addition, the nest-like CNT@Cem could further increase the formation of CNT-CNT junctions against the commercial CNTs and other conductive fillers. Therefore, the breakages/formations of CNT junctions and variations in tunnelling resistance upon deformation are more likely. Furthermore, different from other single-scale fillers, the intrinsic resistance of the hierarchically structured CNT@Cem as a whole would change, resulting in the ultrahigh sensitivity of the SSCCs. The change of intrinsic resistance of CNT@Cem may further improve the sensitivity of the SSCCs with filler content being much higher than the percolation threshold, i.e., the CNT@Cem-25 contains an additional capacitance effect. The increase in capacitance effect has been proved a positive factor in terms of sensitivity [85,86].

Furthermore, the stability and repeatability of the SSCCs with CNT@Cem were evaluated under 10 cycles of repetitive compression with an amplitude of 10 MPa and a loading rate of 0.1 Hz (**Figure S3**). Under cyclic compression, the FCR of all SSCCs steadily increased upon compression and then symmetrically decreased during unloading in each cycle. At the same time, the FCR of the control still demonstrated a sustained decay over time due to the remaining polarization influence. The SSCCs with CNT@Cem all exhibited excellent repeatability in response to the cyclic compression, as evidenced by the constant maximum FCR value in each cycle. In addition, the stress sensitivity of each sample increased with increasing CNT@Cem content and reached the maximum at 25 wt.%, which is consistent with the results of monotonic compression. The excellent self-sensing performance indicates the uniform dispersion of CNTs in the composites [19,25,87]. To further investigate the repeatability of self-sensing behavior, the CNT@Cem-25 sample taken as representative was dynamically compressed at different frequencies (0.05, 0.1, 0.2, 0.5, and 1 Hz at 12.5 MPa, **Figure 8**a) and different stress amplitudes (2.5, 5, 7.5, 10 and 12.5 MPa at 0.1 Hz, **Figure 8**b). The CNT@Cem-25 sample demonstrated stable and consistent cyclic responses and outstanding adaptability to various applied conditions. **Figure 8**c shows the stability of the CNT@Cem-25 sample evaluated by 1000 cyclic compression with an amplitude of 10 MPa and a frequency of 0.1 Hz. It can be observed that the response became almost constant after only several cycles, indicating excellent stability of the self-sensing property of the CNT@Cem-25 sample. To further describe the stability, the peak value at 0 MPa and 10 MPa for each cycle was counted and statistically analyzed using a box plot at a 95% confidence level (**Figure 8**d). The responses to loading (10 MPa) and unloading (0 MPa) showed no statistically significant changes during the 1000 cycles. Only 2 outliers (outside 1.5 times the interquartile range) and 4 outliers were observed with respect to loading and unloading, respectively. This indicated that the CNT@Cem-25 sample has exceptionally high quality in terms of stability and repeatability. In addition, good durability of the sensing performance was observed over a long period of 13 months (**Figure S4**).

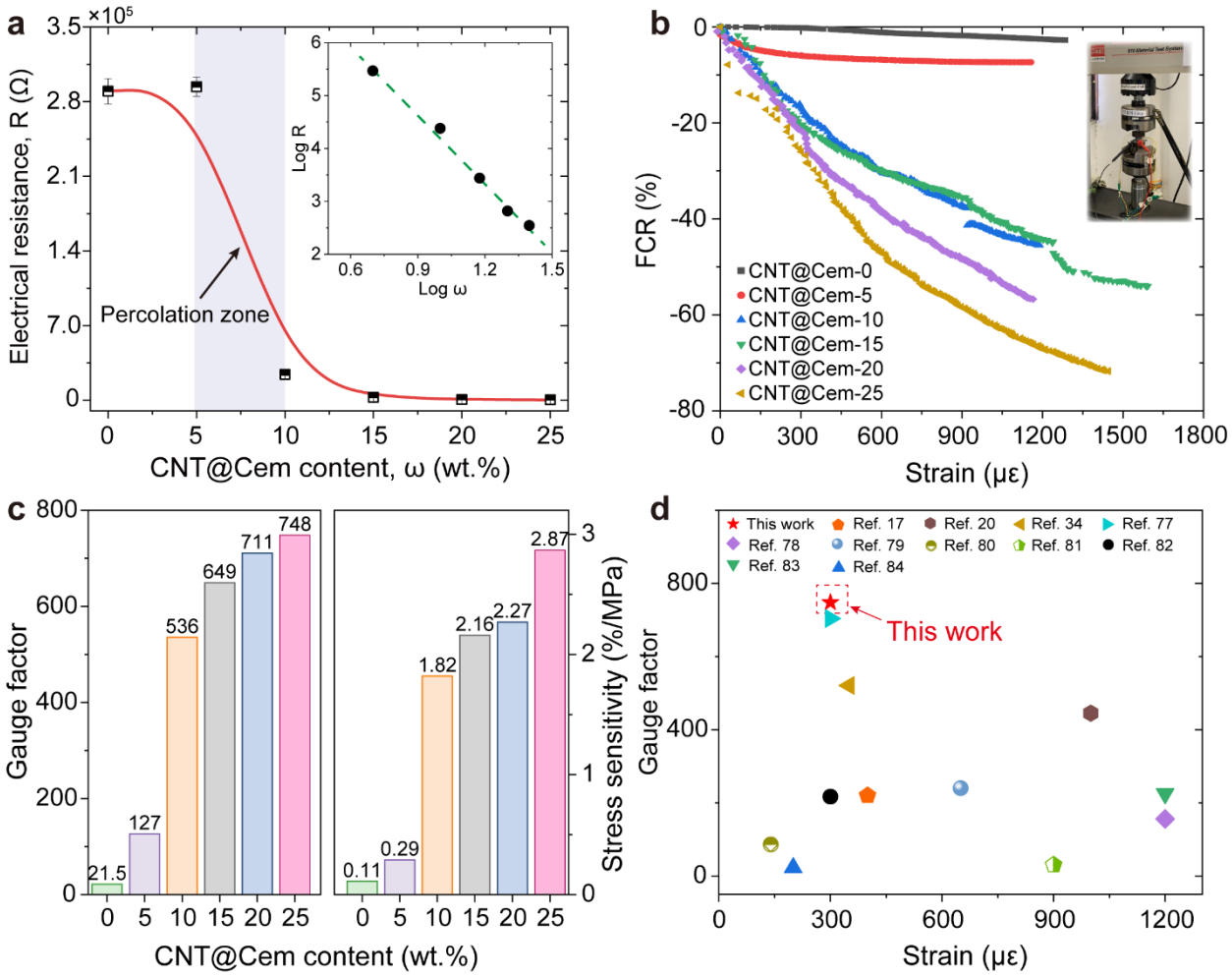

Figure 7. (a) Electrical resistance of the SSCCs with CNT@Cem as a function of CNT@Cem content. Inset shows log-log plot. (b) FCR *versus* Strain for SSCCs with CNT@Cem under monotonic compression with an amplitude of 25 MPa. (c) Gauge factor and stress sensitivity of SSCCs with different CNT@Cem contents. (d) Comparison of the gauge factor of the SSCCs with CNT@Cem-25 with the reported SSCCs with different conductive fillers [17,20,34,77–84].

Figure 8e shows the electrical resistance response of the CNT@Cem-25 sample to the constant loadings from 0 MPa to 25 MPa for a period of 2 min. It is noticed that the resistance instantaneously decreased when the compression was applied and was unchanged when the compression remained constant. The response time of the CNT@Cem-25 sample upon compression was estimated as less than 0.2 s if excluding the loading time (about 4.3 s) (**Figure 8**e, inset). In addition, the recovery time was less than 0.59 s by releasing a 25 MPa compression. Note that there was only a slight difference between the resistance after release (238 Ω) and the initial resistance (241 Ω), which could be understood by the plastic deformation of the sample in

compression. It can be concluded that the CNT@Cem, as a new type of functional filler, has a great potential in the fabrication of SSCCs with the advantages of tailored design, scalable manufacturing, high cost-efficiency, ultra-high sensitivity, excellent robustness, ultra-fast response, and recovery, which significantly expands the practical applications in the fields of SHM and traffic detection.

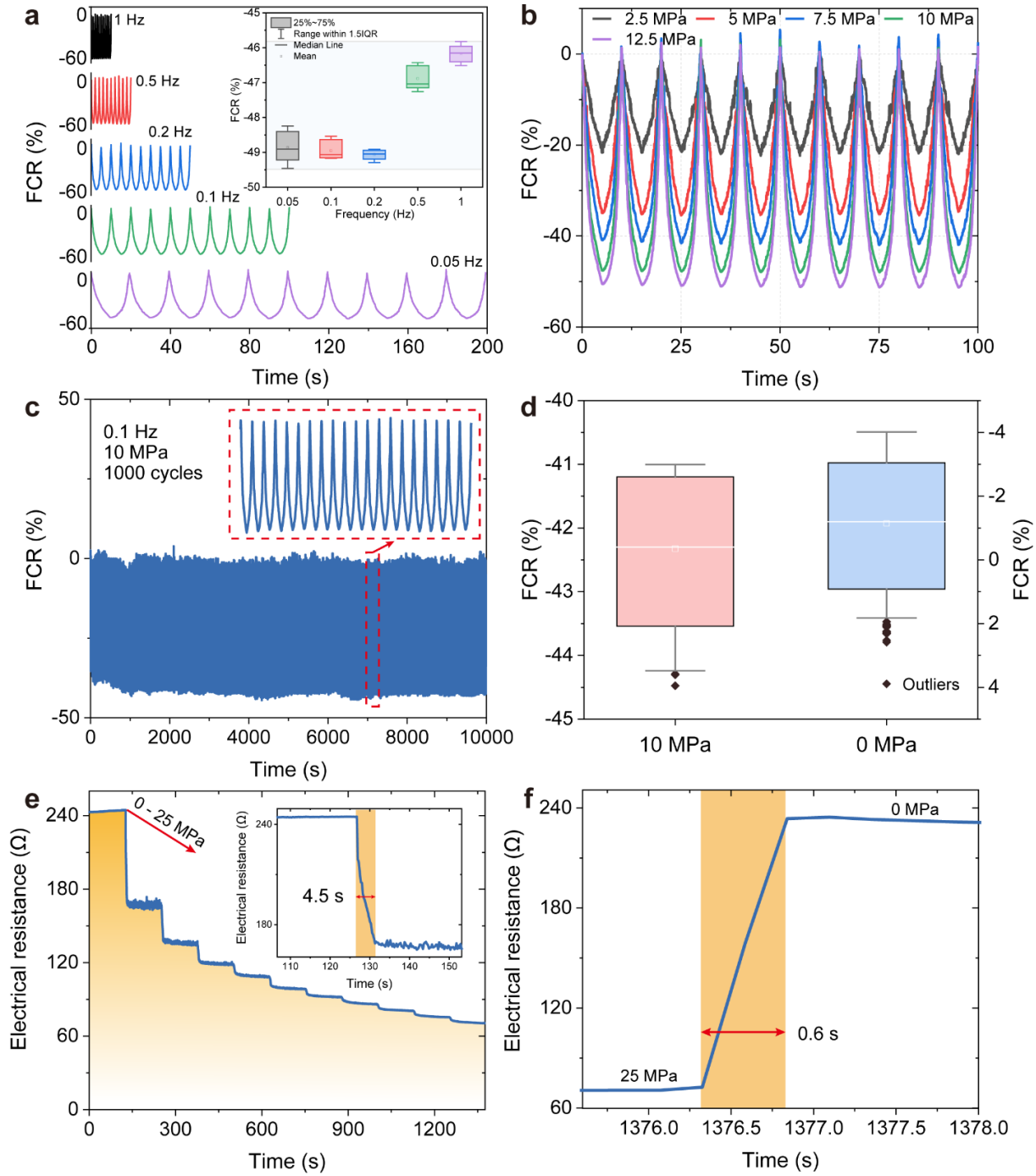

Figure 8. Self-sensing properties of the CNT@Cem-25. (a) FCR under cyclic compression at frequencies of 0.05, 0.1, 0.2, 0.5 and 1 Hz with a stress amplitude of 12.5 MPa. Inset shows FCR *versus* frequency. (b) FCR under cyclic compression at stress amplitudes of 2.5, 5, 7.5, 10, and 12.5 MPa with a frequency of 0.1 Hz. (c) FCR under 10 MPa cyclic compression at a frequency of 0.1 Hz for 1000 cycles. (d) Evaluation of the CNT@Cem-25 composite stability by counted peak values at 0 MPa and 10 MPa, at a 95% confidence level. (e) Electrical resistance change under constant loadings from 0 - 25 MPa for a period of 2 min. Inset shows response time under 1 MPa compression. (f) Recovery time after 25 MPa compression.

3.5. Feasibility verification to develop SSCCs-engineered smart high-speed rail infrastructures

Benefiting from the excellent self-sensing performance and favorable compatibility with HSR concrete track slabs, SSCCs with CNT@Cem could be potentially applied as smart components/structures for HSR monitoring. Here, we devised a monitoring system integrated with an SSCCs-engineered smart track slab using SSCCs with 10 wt.% CNT@Cem and presented preliminary study research for monitoring railway footprints of high-speed trains. The devised smart monitoring system was implemented on a real HSR line (Shanghai-Hangzhou High-speed Railway, K005, China), as shown in **Figure 9**a. There are two types of high-speed trains, including CRH380A and CRH380BL, in service in the test line. **Table S3** lists the principal differences between the two trains.

Figures 9b, c show the typical traces obtained at the 8-car and 16-car high-speed train passages, respectively. Each bogie passing through the SSCCs-engineered smart track slab was clearly identified as a sharp peak of voltage change in the trace. It is easy to obtain the train type circulating in the network by counting the number of successive sharp peaks. The SSCCs-engineered smart track slab has been employed as an axle counter for thousands of train passages and has never observed any faults. However, the individual wheel in each bogie was unable to be identified from the peak since the wheelbase is short, and the SSCCs-engineered smart track slab was constantly compressed during the bogie passing. In addition, the voltage change of the train passage was not very significant because the sensor was installed aside from the rail, on the shoulder of the track slab, and between two sleepers along the rail direction. The maximum dynamic compressive stress (lower than 1 MPa) at such a position should be several times lower than that under the fastener in contact with the rail, according to the theoretical and finite element analyses on the dynamic response of vehicle-track coupling system [88-90]. Further improvement will be achieved by considering the optimal layout of SSCCs in high-speed rail infrastructures.

After identifying the train type and given that the distances between bogie centers are known for each type of train, the instantaneous and average train speed can be simply obtained. In addition, by comparing the first car's instantaneous speed and the last car's instantaneous speed, the acceleration of the whole train can be distinguished. **Table 1** gives the train speeds calculated using the two traces in **Figure 9**. It can be seen that the average speeds of the two trains stand exactly between the first car's instantaneous speed and the last car's instantaneous speed. The

train, CRH380A, entered the instrumented sector decelerating but left the sector accelerating, which is the opposite of the train, CRH380BL. Also, we can find that the peak amplitude corresponding to each bogie was different due to the different weight of each car, indicating that the SSCCs-engineered smart track slab can be used for train dynamic load estimation. In this way, excessive load that causes degradation in the trains and the railway infrastructure would be refrained. However, customized design, installation, and calibration of the SSCCs-engineered smart track slab are still needed for its precise measurement of trainload in the future application.

Table 1. Average and instantaneous speeds of the two trains.

Train type	Average speed (km/h)	Instantaneous speed of the first car (km/h)	Instantaneous speed of last car (km/h)	Sign of acceleration
CRH380A	34.67	34.99	33.16	-
CRH380BL	43.33	41.58	44.52	+

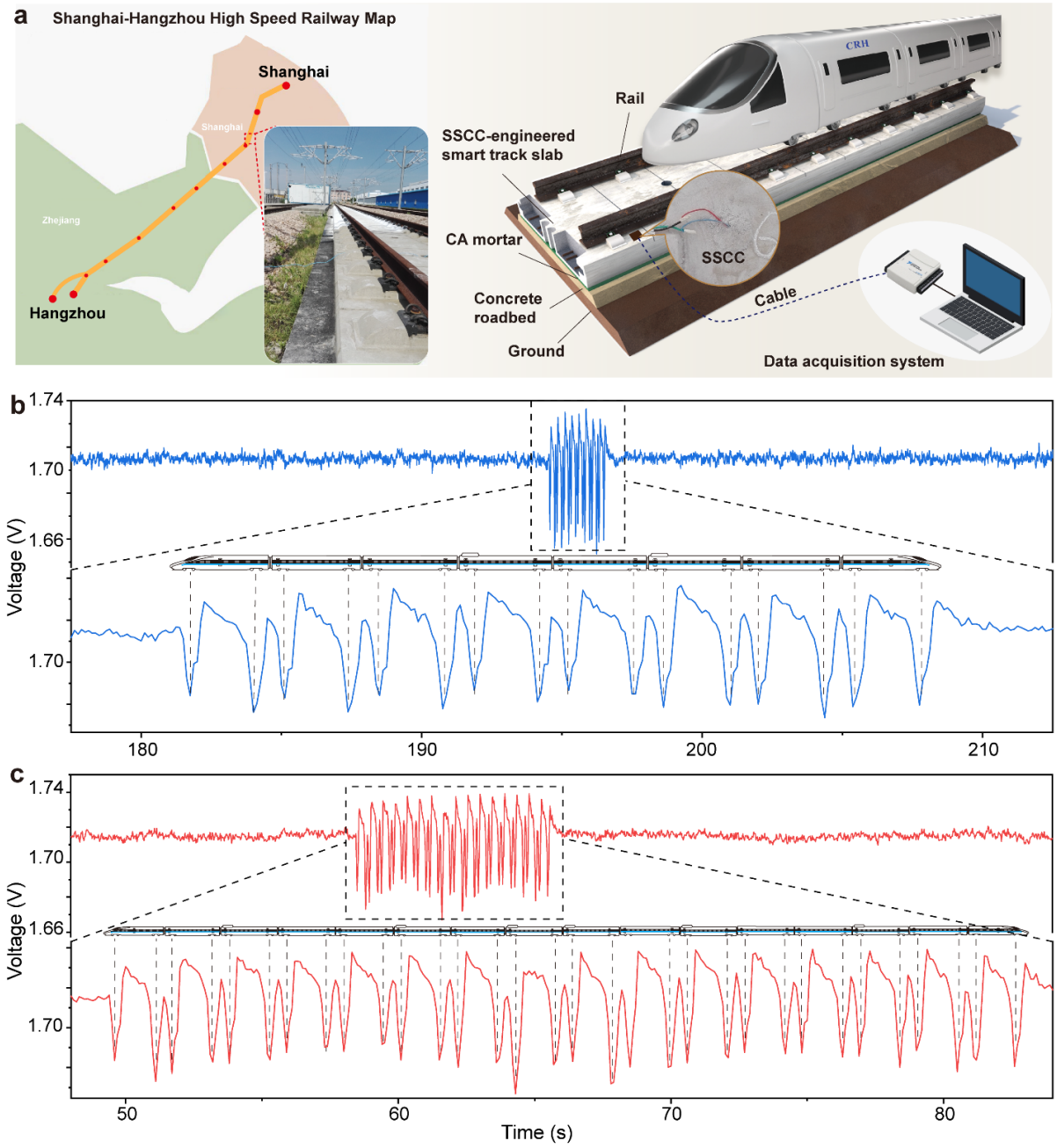

Figure 9. SSCCs-engineered smart track slab for high-speed rail monitoring. (a) Schematic of test site and setup. (b) Representative response to an 8-car high-speed train passage. (c) Representative response to a 16-car high-speed train passage.

4. Conclusions

The paper has reported a fabrication method for next-generation SSCCs comprising a hierarchically structured functional filler, which can alleviate the CNT's dispersion problem and

enable scalable manufacturing of SSCCs with outstanding self-sensing performance. The hierarchically structured CNT@Cem composite filler was *in-situ* CVD synthesized by directly growing CNTs on cement particles. The as-synthesized nest-like CNT@Cem structure processed enhanced specific surface area and reduced gypsum content, thus providing abundant nucleation sites for cement products formation and accelerating early-age hydration of the SSCCs. In addition, the CNT@Cem led to the excessive formation of highly oriented CH crystals around while reducing the amount of C-S-H gel, thus less formation of hydration products that contribute to the strength of the SSCCs with CNT@Cem. The addition of CNT@Cem can effectively tailor the electrical microstructures, thus enhancing the electrical conductivity of the SSCCs. The nest-like CNT@Cem significantly enhanced the sensitivity of the SSCCs. Increasing CNT@Cem content can continuously improve the sensitivity, achieving a maximum stress sensitivity of 2.87 %/MPa and the gauge factor of 748 for the CNT@Cem-25 sample. The CNT@Cem also demonstrated excellent repeatability and stability, outstanding adaptability to various applied conditions, fast response and recovery, showing great potential for practical applications in long-term and real-time HSR infrastructure monitoring. Future work will focus on the performance modulation of SSCCs with CNT@Cem synthesized under different CVD regimes and catalysts to identify how the hierarchical structures' morphologies (i.e., length, diameter, and density) produced affect the resultant SSCC's performance. The underlying growth mechanism will be further verified by the *in-situ* growing of CNTs on individual cement components such as cement clinker, gypsum, C_3S, and C_3A. Besides cement particles, supplementary cementitious materials such as fly ash, silica fume, and fine and coarse aggregates would be promising alternatives for CNT growth support. More efforts are needed to integrate and optimize the synthesis process of CNTs on these supplementary cementitious materials with the traditional cement manufacturing of processes to realize mass production, energy saving, and cost reduction. In addition, the evaluation of CNT@Cem cost as well as SSCCs' and their smart HSR infrastructures' life cycle cost should be considered emphatically.

Acknowledgments

The work described in this paper is partially supported by the grants from the National

635 Science Foundation of China (51978127 and 51578110), a grant from The Hong Kong
636 Polytechnic University (Project No.: 1-BBAG), and a grant from the Research Grants Council of
637 the Hong Kong Special Administrative Region, China (Project No. T22-502/18-R). The authors
638 appreciate the funding support by the Chinese National Engineering Research Centre on Rail
639 Transit Electrification and Automation (Hong Kong Branch) of the Hong Kong Polytechnic
640 University. Thanks are due to Prof. Yanbin Cui at Chinese Academy of Sciences, Prof. Xufeng
641 Dong at Dalian University of Technology, and Dr. Peigang Li at Shanghai Institute of
642 Technology for their assistance with the experiments, and to Prof. Xun Yu at New York Institute
643 of Technology for valuable discussions.
644

645 **References**

646 [1] R. Clark, *NDT & E International* **2004**, *37*, 111.
647 [2] J. Wang, X.-Z. Liu, Y.-Q. Ni, *Computer-Aided Civil and Infrastructure Engineering*
648 **2018**, *33*, 21.
649 [3] M. L. Filograno, P. C. Guillen, A. Rodriguez-Barrios, S. Martin-Lopez, M. Rodriguez-
650 Plaza, Á. Andres-Alguacil, M. Gonzalez-Herraez, *IEEE Sensors Journal* **2012**, *12*, 85.
651 [4] S. Ding, S. Dong, A. Ashour, B. Han, *Journal of Applied Physics* **2019**, *126*, 241101.
652 [5] B. Han, S. Ding, X. Yu, *Measurement* **2015**, *59*, 110.
653 [6] B. Han, L. Zhang, J. Ou, *Smart and Multifunctional Concrete toward Sustainable*
654 *Infrastructures*. Springer Singapore, **2017**.
655 [7] D. Dimov, I. Amit, O. Gorrie, M. D. Barnes, N. J. Townsend, A. I. S. Neves, F. Withers,
656 S. Russo, M. F. Craciun, *Advanced Functional Materials* **2018**, *28*, 1705183.
657 [8] M. Krystek, A. Ciesielski, P. Samorì, *Advanced Functional Materials* **2021**, *31*, 2101887.
658 [9] O. Galao, F. J. Baeza, E. Zornoza, P. Garcés, *Cement and Concrete Composites* **2014**, *46*,
659 90.
660 [10] E. García-Macías, F. Ubertini, *Earthquake Engineering & Structural Dynamics* **2019**, *48*,
661 548.
662 [11] S. Ding, Y.-W. Wang, Y.-Q. Ni, B. Han, *Smart Materials and Structures* **2020**, *29*,
663 055013.
664 [12] S. Ding, C. Xu, Y.-Q. Ni, B. Han, *Smart Materials and Structures* **2021**, *30*, 065010.
665 [13] B. Han, X. Yu, E. Kwon, *Nanotechnology* **2009**, *20*, 445501.
666 [14] G. Jing, M. Siahkouhi, J. Riley Edwards, M. S. Dersch, N. A. Hoult, *Construction and*
667 *Building Materials* **2021**, *271*, 121533.
668 [15] S. J. Lee, D. Ahn, I. You, D. Y. Yoo, Y. S. Kang, *Automation in Construction* **2020**, *119*,
669 103323.
670 [16] B. Han, X. Yu, J. Ou, *Self-Sensing Concrete in Smart Structures*, Elsevier, **2014**.
671 [17] A. L. Materazzi, F. Ubertini, A. D'Alessandro, *Cement and Concrete Composites* **2013**,
672 *37*, 2.

673 [18] S. Dong, D. Wang, A. Ashour, B. Han, J. Ou, *Composites Part A: Applied Science and*
674 *Manufacturing* **2021**, *141,* 106228.
675 [19] G. Y. Li, P. M. Wang, X. Zhao, *Cement and Concrete Composites* **2007**, *29*, 377.
676 [20] F. Azhari, N. Banthia, *Cement and Concrete Composites* **2012**, *34*, 866.
677 [21] M. F. L. De Volder, S. H. Tawfick, R. H. Baughman, A. J. Hart, *Science* **2013**, *339*, 535.
678 [22] A. P. Kumar, D. Depan, N. Singh Tomer, R. P. Singh, *Progress in Polymer Science* **2009**,
679 *34*, 479.
680 [23] A. Sobolkina, V. Mechtcherine, V. Khavrus, D. Maier, M. Mende, M. Ritschel, A.
681 Leonhardt, *Cement and Concrete Composites* **2012**, *34*, 1104.
682 [24] S. Parveen, S. Rana, R. Fangueiro, M. C. Paiva, *Cement and Concrete Research* **2015**, *73*,
683 215.
684 [25] B. Han, S. Sun, S. Ding, L. Zhang, X. Yu, J. Ou, *Composites Part A: Applied Science and*
685 *Manufacturing* **2015**, *70,* 69-81.
686 [26] S. J. Chen, C. Y. Qiu, A. H. Korayem, M. R. Barati, W. H. Duan, *Powder Technology*
687 **2016**, *301*, 412.
688 [27] S. Banerjee, T. Hemraj-Benny, S. S. Wong, *Advanced Materials* **2005**, *17*, 17.
689 [28] H. Park, J. Zhao, J. P. Lu, *Nano Letters* **2006**, *6*, 916.
690 [29] S. W. Kim, T. Kim, Y. S. Kim, H. S. Choi, H. J. Lim, S. J. Yang, C. R. Park, *Carbon*
691 **2012**, *50*, 3.
692 [30] B. Han, S. Ding, S. Sun, L. Zhang, J. Ou, In *Chemical Functionalization of Carbon*
693 *Nanomaterials* (Ed.: Thakur, V. K.), CRC Press, **2015**, pp. 748–773.
694 [31] C. He, N. Zhao, C. Shi, E. Liu, J. Li, *Advanced Materials* **2015**, *27*, 5422.
695 [32] S. Sun, X. Yu, B. Han, J. Ou, *Construction and Building Materials* **2013**, *49*, 835.
696 [33] M. Zhan, G. Pan, F. Zhou, R. Mi, S. P. Shah, *Cement and Concrete Composites* **2020**,
697 *108*, 103518.
698 [34] L. Zhang, S. Ding, L. Li, S. Dong, D. Wang, X. Yu, B. Han, *Composites Part A: Applied*
699 *Science and Manufacturing* **2018**, *109*, 303.
700 [35] Z. Liu, J. Wang, V. Kushvaha, S. Poyraz, H. Tippur, S. Park, M. Kim, Y. Liu, J. Bar, H.
701 Chen, X. Zhang, *Chemical Communications* **2011**, *47*, 9912.
702 [36] J. Foroughi, G. M. Spinks, D. Antiohos, A. Mirabedini, S. Gambhir, G. G. Wallace, S. R.
703 Ghorbani, G. Peleckis, M. E. Kozlov, M. D. Lima, R. H. Baughman, *Advanced Functional*
704 *Materials* **2014**, *24*, 5859.
705 [37] M. Kumar, Y. Ando, *Journal of Nanoscience and Nanotechnology* **2010**, *10*, 3739.
706 [38] A. G. Nasibulin, S. D. Shandakov, L. I. Nasibulina, A. Cwirzen, P. R. Mudimela, K.
707 Habermehl-Cwirzen, D. A. Grishin, Y. V. Gavrilov, J. E. M. Malm, U. Tapper, Y. Tian, V.
708 Penttala, M. J. Karppinen, E. I. Kauppinen, *New Journal of Physics* **2009**, *11*, 23013.
709 [39] P. Ludvig, J. M. Calixto, L. O. Ladeira, I. C. P. Gaspar, *Materials* **2010**, *4*, 575.
710 [40] F. Ghaharpour, A. Bahari, M. Abbasi, A. A. Ashkaran, *Construction and Building*
711 *Materials* **2016**, *113*, 523.
712 [41] C. Warakulwit, S. Yadnum, V. Paluka, O. Phuakkong, M. Niamlaem, K.
713 Pongpaisanseree, S. Sinthupinyo, J. Limtrakul, *Chemical Engineering Journal* **2015**, *278*, 150.
714 [42] T. Buasiri, K. Habermehl-Cwirzen, L. Krzeminski, A. Cwirzen, *Nanomaterials* **2019**, *9*,
715 594.
716 [43] P. R. Mudimela, L. I. Nasibulina, A. G. Nasibulin, A. Cwirzen, M. Valkeapää, K.
717 Habermehl-Cwirzen, J. E. M. Malm, M. J. Karppinen, V. Penttala, T. S. Koltsova, O. V.

718 Tolochko, E. I. Kauppinen, *Journal of Nanomaterials* **2009**, *2009*, 29.
719 [44] A. G. Nasibulin, T. Koltsova, L. I. Nasibulina, I. V. Anoshkin, A. Semencha, O. V.
720 Tolochko, E. I. Kauppinen, *Acta Materialia* **2013**, *61*, 1862.
721 [45] W. Brockner, C. Ehrhardt, M. Gjikaj, *Thermochimica Acta* **2007**, *456*, 64.
722 [46] C. Stephens, L. Brown, F. Sanchez, *Carbon* **2016**, *107*, 482.
723 [47] D. He, M. Bozlar, M. Genestoux, J. Bai, *Carbon* **2010**, *48*, 1159.
724 [48] S. Helveg, C. López-Cartes, J. Sehested, P. L. Hansen, B. S. Clausen, J. R. Rostrup-
725 Nielsen, F. Abild-Pedersen, J. K. Nørskov, *Nature* **2004**, *427*, 426.
726 [49] S. Hofmann, R. Sharma, C. Ducati, G. Du, C. Mattevi, C. Cepek, M. Cantoro, S. Pisana,
727 A. Parvez, F. Cervantes-Sodi, A. C. Ferrari, R. Dunin-Borkowski, S. Lizzit, L. Petaccia, A.
728 Goldoni, J. Robertson, *Nano Letters* **2007**, *7*, 602.
729 [50] L. Fan, P. F. Liu, X. Yan, L. Gu, Z. Z. Yang, H. G. Yang, S. Qiu, X. Yao, *Nature*
730 *Communications* **2016**, *7*, 10667.
731 [51] A. T. Phan, M. K. Paek, Y. B. Kang, *Acta Materialia* **2014**, *79*, 1.
732 [52] A. Rinaldi, N. Abdullah, M. Ali, A. Furche, S. B. Abd. Hamid, D. S. Su, R. Schlögl,
733 *Carbon* **2009**, *47*, 3023.
734 [53] M. Pérez-Cabero, E. Romeo, C. Royo, A. Monzón, A. Guerrero-Ruíz, I. Rodríguez-
735 Ramos, *Journal of Catalysis* **2004**, *224*, 197.
736 [54] N. Latorre, E. Romeo, J. I. Villacampa, F. Cazaña, C. Royo, A. Monzón, *Catalysis Today*
737 **2010**, *154*, 217.
738 [55] N. Prieto-Taboada, O. Gómez-Laserna, I. Martínez-Arkarazo, M. Á. Olazabal, J. M.
739 Madariaga, *Analytical Chemistry* **2014**, *86*, 10131.
740 [56] S. S. Potgieter-Vermaak, J. H. Potgieter, R. Van Grieken, *Cement and Concrete Research*
741 **2006**, *36*, 656.
742 [57] T. Schmid, P. Dariz, *Journal of Raman Spectroscopy* **2015**, *46*, 141.
743 [58] M. J. Bronikowski, *Carbon* **2006**, *44*, 2822.
744 [59] I. Pane, W. Hansen, *Cement and Concrete Research* **2005**, *35*, 1155.
745 [60] D. Venegoni, P. Serp, R. Feurer, Y. Kihn, C. Vahlas, P. Kalck, *Carbon* **2002**, *40*, 1799.
746 [61] A. Magrez, J. W. Seo, C. Mikó, K. Hernádi, L. Forró, *Journal of Physical Chemistry B*
747 **2005**, *109*, 10087.
748 [62] W. D. Zhang, Y. Wen, S. M. Liu, W. C. Tjiu, G. Q. Xu, L. M. Gan, *Carbon* **2002**, *40*,
749 1981.
750 [63] B. Han, S. Ding, J. Wang, J. Ou, *Nano-Engineered Cementitious Composites*, Springer
751 Singapore, **2019**.
752 [64] J. M. Makar, G. W. Chan, *Journal of the American Ceramic Society* **2009**, *92*, 1303.
753 [65] Z. Li, D. J. Corr, B. Han, S. P. Shah, *Cement and Concrete Composites* **2020**, *107*,
754 103513.
755 [66] M. Tafesse, H. K. Kim, *Composites Part B: Engineering* **2019**, *169*, 55.
756 [67] P. Stynoski, P. Mondal, C. Marsh, *Cement and Concrete Composites* **2015**, *55*, 232.
757 [68] F. Moulin, M. Devel, S. Picaud, *Physical Review B* **2005**, *71*, 165401.
758 [69] M. S. Konsta-Gdoutos, Z. S. Metaxa, S. P. Shah, *Cement and Concrete Research* **2010**,
759 *40*, 1052.
760 [70] V. S. Harutyunyan, E. S. Abovyan, P. J. M. Monteiro, V. P. Mkrtchyan, M. K. Balyan, A.
761 P. Aivazyan, *Journal of the American Ceramic Society* **2003**, *86*, 2162.
762 [71] X. Cui, B. Han, Q. Zheng, X. Yu, S. Dong, L. Zhang, J. Ou, *Composites Part A: Applied*

Science and Manufacturing **2017**, *103*, 131.
[72] P. C. Hewlett, M. Liska, *Lea's chemistry of cement and concrete*, Elsevier, **2019**.
[73] R. K. Abu Al-Rub, A. I. Ashour, B. M. Tyson, *Construction and Building Materials* **2012**, *35*, 647.
[74] S. Musso, J.-M. M. Tulliani, G. Ferro, A. Tagliaferro, *Composites Science and Technology* **2009**, *69*, 1985.
[75] B. Han, L. Zhang, S. Zeng, S. Dong, X. Yu, R. Yang, J. Ou, *Composites Part A: Applied Science and Manufacturing* **2017**, *95*, 100.
[76] M. Saafi, *Nanotechnology* **2009**, *20*, 395502.
[77] B. Han, L. Zhang, S. Sun, X. Yu, X. Dong, T. Wu, J. Ou, *Composites Part A: Applied Science and Manufacturing* **2015**, *79*, 103.
[78] S. Sun, S. Ding, B. Han, S. Dong, X. Yu, D. Zhou, J. Ou, *Composites Part B: Engineering* **2017**, *129*, 221.
[79] C. Camacho-Ballesta, E. Zornoza, P. Garcés, *Advances in Cement Research* **2016**, *28*, 274.
[80] P. A. Danoglidis, M. S. Konsta-Gdoutos, E. E. Gdoutos, S. P. Shah, *Construction and Building Materials* **2016**, *120*, 265.
[81] A. O. Monteiro, P. B. Cachim, P. M. F. J. Costa, *Cement and Concrete Composites* **2017**, *81*, 59.
[82] L. Zhang, Q. Zheng, X. Dong, X. Yu, Y. Wang, B. Han, *Construction and Building Materials* **2020**, *256*, 119452.
[83] B. Han, Y. Wang, S. Ding, X. Yu, L. Zhang, Z. Li, J. Ou, *Journal of Intelligent Material Systems and Structures* **2017**, *28*, 699.
[84] S. Dong, B. Han, J. Ou, Z. Li, L. Han, X. Yu, *Cement and Concrete Composites* **2016**, *72*, 48.
[85] B. Han, K. Zhang, X. Yu, E. Kwon, J. P. Ou, *Cement and Concrete Composites* **2012**, *34*, 794.
[86] X. Li, M. Li, *Cement and Concrete Research* **2019**, *123*, 105714.
[87] H. K. Kim, I. S. Park, H. K. Lee, *Composite Structures* **2014**, *116*, 713.
[88] Y. Song, Y. Du, X. Zhang, B. Sun, *Applied Sciences* **2019**, *9*, 4165.
[89] Z. Zeng, J. Wang, S. Shen, P. Li, A. A. Shuaibu, W. Wang, *Construction and Building Materials* **2019**, *210*, 639.
[90] X. Lei, B. Zhang, *Journal of Transportation Engineering.* **2011**, *137*, 227.

Biographies and photos

 **Siqi Ding**	**Siqi DING** obtained his PhD degree from the Hong Kong Polytechnic University in 2021. He is now a postdoctoral fellow at School of Civil and Environmental Engineering, Harbin Institute of Technology, Shenzhen, China. His main research interests include smart materials and structures, structural health monitoring and nanotechnology in building material.
 **Yu Xiang**	**Yu XIANG** is currently a research fellow in the Department of Civil and Environmental Engineering at the Hong Kong Polytechnic University. He received his BEng and Ph.D. degrees in civil engineering from Hunan University. His research centers around the structural application of advanced engineering materials, with focuses on high-performance and durable structures enabled by fiber-reinforced polymer (FRP) and ultra-high-performance concrete (UHPC).
 **Yi-Qing Ni**	**Yi-Qing NI**, male, obtained his Bachelor and Master degrees from Zhejiang University, and PhD degree from The Hong Kong Polytechnic University. He is a chair professor at Department of Civil and Environmental Engineering, The Hong Kong Polytechnic University, and the director of the National Engineering Research Center on Rail Transit Electrification and Automation (Hong Kong Branch), Hong Kong. His research areas cover structural health monitoring, structural dynamics and control, smart materials and structures, sensors and actuators, monitoring and control in rail engineering.
 **Vijay Kumar Thakur**	**Vijay Kumar Thakur** is Professor and Head of the Biorefining and Advanced Materials Research Centre at SRUC, Edinburgh, U.K. He also holds an Adjunct Professor position in Jiangsu University and is a Visiting Professor at Shiv Nadar University, UPES and Visitor at Cranfield University, U.K. His research activities span the disciplines of Biorefining, Chemistry, Manufacturing, Materials Science, Nanotechnology, and Sustainable and Advanced Materials. He has published over 300 SCI journal articles, 2 patents, 50 books, and 40 book chapters.

 **Xinyue Wang**	**Xinyue WANG** obtained his PhD degree from Dalian University of Technology in 2021. He is now a postdoctoral fellow at School of Civil Engineering, Dalian University of Technology, China. His main research interests include nano-engineered cementitious composites and interfaces in concrete materials and structures.
 **Baoguo Han**	**Baoguo HAN** received his PhD in the field of smart materials and structures from the Harbin Institute of Technology, China, in 2005. He is currently a professor of civil engineering in the Dalian University of Technology, China. He was invited to the University of Minnesota and has worked as a visiting research scholar there for 3 years. His main research interests include smart/multifunctional concrete, nano/fiber engineered concrete, structural health monitoring, and traffic detection.
 **Jinping Ou**	**Jinping OU** received his Ph.D. degree from the Harbin Institute of Technology, China, in 1987. He is a professor at both Harbin Institute of Technology and Dalian University of Technology, China. His main research interests include structural damage, reliability and health monitoring, structural vibration and control, smart materials and structures. He has been an academician of Chinese Academy of Engineering since 2003, and was the president of the Chinese Society for Vibration Engineering, the vice-president of the Architectural Society of China, as well as the vice-president and fellow of the International Society for Structural Health Monitoring of Intelligent Infrastructure.

811